Author Manuscript

Author Manuscript

Author Manuscript

Author Manuscript

HHS Public Access

Author manuscript

Science. Author manuscript; available in PMC 2024 July 16.

Published in final edited form as:

Science. 2024 March 29; 383(6690): 1471–1478. doi:10.1126/science.adn1011.

Oxygen imaging of hypoxic pockets in the mouse cerebral cortex

Felix R.M. Beinlich[1,*,†], **Antonios Asiminas**[1,†], **Verena Untiet**[1], **Zuzanna Bojarowska**[1], **Virginia Plá**[1], **Björn Sigurdsson**[1], **Vincenzo Timmel**[2], **Lukas Gehrig**[2], **Michael H. Graber**[2], **Hajime Hirase**[1,3], **Maiken Nedergaard**[1,3,*]

[1]Division of Glial Disease and Therapeutics, Center for Translational Neuromedicine, Faculty of Health and Medical Sciences, University of Copenhagen; 2200 Copenhagen, Denmark

[2]School of Engineering, FHNW University of Applied Sciences and Arts Northwestern Switzerland; 5210 Windisch, Switzerland

[3]Division of Glial Disease and Therapeutics, Center for Translational Neuromedicine, University of Rochester Medical Center; Rochester, NY 14642, USA

Abstract

Consciousness is lost in seconds upon cessation of cerebral blood flow. The brain cannot store oxygen and interruption of oxidative phosphorylation is fatal within minutes. Yet, only rudimentary knowledge exists regarding cortical partial oxygen tension (pO_2) dynamics under physiological conditions. We here introduce Green NanoLuc (GeNL), a genetically encoded bioluminescent oxygen indicator for pO_2 imaging. In awake behaving mice, we uncover the existence of spontaneous, spatially defined “hypoxic pockets” and demonstrate their linkage to the abrogation of local capillary flow. Exercise reduced the burden of hypoxic pockets by 52% compared with rest. The study provides insight into cortical oxygen dynamics in awake behaving animals, concurrently with establishing a new tool to delineate the importance of oxygen tension in physiological processes and neurological diseases.

[*]Corresponding author. felix.beinlich@sund.ku.dk (F.R.M.B.); nedergaard@urmc.rochester.edu (M.N.).
[†]These authors contributed equally to this work

Author contributions:
Conceptualization: FRMB, HH, MN
Methodology: FRMB, AA, VU, ZB, VP, VT, LG, BS, MG, HH, MN
Software: AA, FRMB, BS, VT, LG, MG
Formal analysis: FRMB, AA, VP, ZB, VT, LG, MG, BS
Investigation: FRMB, ZB
Visualization: FRMB, AA
Funding acquisition: HH, MN, VU, AA
Project administration: FRMB, MN
Supervision: FRMB, MG, HH, MN
Writing – original draft: FRMB, AA, HH, MN
Writing – review & editing: FRMB, AA, HH, MN

Competing interests: Authors declare that they have no competing interests.

Supplementary Materials
Materials and Methods
Figs. S1 to S16
Tables S1 to S2
References (59–66)
Movies S1 to S4

Author Manuscript Author Manuscript Author Manuscript Author Manuscript

One-Sentence Summary:

GeNL bioluminescence imaging detects behavioral-dependent transient “hypoxic pockets” in the mouse brain.

Cerebral partial oxygen tension (pO_2)

The human brain consumes approximately 20% of total body oxygen consumption at rest (1–3). Delivery and demand of oxygen (O_2) are so finely balanced that maintaining tissue oxygenation may be the most critical of all brain functions. Yet, our understanding of the dynamics of brain tissue oxygen tension (pO_2) under physiological conditions remains limited, largely due to the lack of spatially precise measurement techniques for pO_2 imaging. Currently, tissue pO_2 can be measured by phosphorescence and by Clark-type electrodes (4, 5). Neither approach provides sufficient high spatio-temporal sensitivity to detect physiological changes in cortical pO_2.

We here developed a methodology to measure relative changes in pO_2 utilizing the oxygen-dependent reaction of a luminescent substrate guided by its enzyme expressed in astrocytes. This method has a superior signal-to-noise ratio due to its bioluminescence origin and a spatio-temporal resolution that can visualize the dynamics of cortical pO_2 in awake behaving mice. Green NanoLuc (GeNL) is a luminescent fusion protein consisting of the luciferase NanoLuc (6) and the fluorescent protein mNeongreen (7). During the enzymatic conversion of its luminescent substrate furimazine to furimamide energy is emitted in the form of light (6). The fluorescent fusion protein acts as a fluorescence amplifier increasing the quantum yield via Förster resonance energy transfer (FRET). The enzymatic reaction of GeNL with furimazine depends on O_2 (Fig. 1A) and the intensity of the bioluminescence signal is linearly correlated to the availability of O_2 when O_2 is the rate-limiting factor in the enzymatic reaction (8).

Green NanoLuc can detect oxygen in mouse cortex

To assess whether the oxygen-dependency can be used *in vivo* to visualize spontaneous pO_2 dynamics in the brain, we expressed GeNL in cortical astrocytes of wildtype mice (fig. S1A) and measured bioluminescence intensity (BLI) after topical administration of the substrate furimazine via a cranial window (Fig. 1A–B and fig. S2A–B). BLI follows cerebral pO_2, when O_2 concentration of the breathing air was changed stepwise ranging 10% – 40% under ketamine/xylazine (KX) anesthesia. The baseline level of air O_2 was kept at 20% and then changed for one-minute periods followed by a one-minute recovery phase at baseline levels (Fig. 1C). Changing the O_2 concentration from 20% to 40% increased BLI by ~200%, whereas a reduction of O_2 concentration in the inhaled air to 10% decreased BLI by ~50% from baseline. (Fig. 1D–E, fig. S3A, and Movie S1). To record the absolute pO_2 in the BLI imaging field, we placed an O_2-sensitive Clark-type microelectrode in the field of view during the calibration protocol (Fig. 1B). Cerebral pO_2 increased by 20 mmHg at 30% O_2, 50 mmHg at 40% O_2, and reduced by 10 mmHg from baseline at 10% O_2 (Fig. 1D–E and fig. S3A). The reaction time and slope of BLI occurred in parallel with the electrode recordings indicating similar reaction times with no time-lag between change

Author Manuscript Author Manuscript Author Manuscript Author Manuscript

in O_2 and change in BLI (fig. S3B–C). BLI peaked faster than electrode recordings upon increase of O_2 concentration but declined at similar rate when O_2 was lowered, perhaps indicating substrate availability limitations under conditions with unphysiologically high O_2 concentrations (fig. S3D). ΔBLI is correlated with ΔpO_2 in a linear manner (Fig. 1F), although availability of free O_2 might limit the sensitivity at low O_2 supply. GeNL BLI is thus an accurate measure of relative pO_2.

Increased metabolism leads to increased carbon dioxide (CO_2) concentrations as a byproduct of cellular respiration. CO_2 is a known vasodilator and alters pH (9, 10). We thus investigated the pH change in brain tissue upon O_2 calibration to exclude pH alterations causing the effect on BLI described above. Mice expressing the genetically encoded fluorescent pH sensor pHuji (11) in the extracellular space were implanted with a fiber photometry probe and exposed to the same protocol for O_2 calibration under KX anesthesia. Manipulating O_2 did not alter pH during O_2 calibration (fig. S4 A–C).

Activation of the whisker barrel cortex by contralateral whisker stimulation leads to an increase in local blood flow and an increase in pO_2. We next imaged the whisker barrel cortex in awake behaving mice while stimulating the whiskers by air puffs to test if BLI can detect the sensory-induced cortical pO2 change. Mice were exposed to a series of ten brief whisker stimulations (5 Hz, 50 ms duration for 10 s, 50 s inter-stimulation interval) (Fig. 1G) (12). During whisker stimulation BLI increased in the field of view (FOV) (Fig. 1H and Movie S2) closely following the individual series of whisker stimulation trials (Fig. 1I). Moreover, KX-anesthetized mice with simultaneous O_2 microelectrode recording showed similar consistent correlation between BLI and ΔpO_2 (fig. S5A–E). Notably, the amplitude and the timing of BLI response differed between awake and KX anesthetized mice (fig. S6A–G), supporting the notion that anesthesia dampens tissue pO_2 and functional hyperemia dynamics (13, 14).

Oxygen dynamics in the cerebral cortex

Continuous imaging of BLI showed that pO_2 under resting conditions was highly dynamic, exhibiting local transient dips in pO_2 (Fig. 2A–C and Movie S3). These local hypoxic events were spatially constricted, lasting several seconds up to minutes and typically showed a sharp on- and offset in relative tissue pO_2 (Fig. 2 C–E). Due to their negative relative amplitude in pO_2 and the characteristic sharply defined border, we named them ‘hypoxic pockets’.

Hypoxic pockets were identified based on their negative amplitude (pO_2(ΔB/B)), typical sharp on- and offset, clear edges, and long duration (fig. S7A And Movie S4).
Hypoxic pockets were observed throughout 20-minute-long recordings (Fig. 2F–H). In KX anesthetized mice, 200 ± 22 hypoxic pockets (Mean ± SEM) were detected during this time (Fig. 2I). Within a single frame recorded at 1 Hz 8.12 ± 0.04 hypoxic pockets were observed per mm^2 covering 2.43 ± 0.02% of the field of view (Fig. 2J–K). Hypoxic pockets covered an area of 1823 ± 27 μm^2 while lasting 48.2 ± 1.0 seconds (Fig. 2L–M). pO_2(ΔB/B) decreased by 27.2 ± 4.5% from baseline prior to each hypoxic pocket (Fig. 2N). Hypoxic pockets had an average diameter of 45.29 ± 0.31 μm and an almost circular shape (Fig.

Author Manuscript Author Manuscript Author Manuscript Author Manuscript

2O–P). Hypoxic pockets often occurred repeatedly in the same area. Within a 20-minute recording on average 73.2 ± 5.1 of those regions (ROIs) were detected with on average 2.8 ± 0.1 hypoxic pockets (Fig. 2Q–R). Each minute 0.15 ± 0.01 hypoxic pockets occurred within a given ROI, meaning that every ~ 7 minutes a hypoxic pocket occurred at the same place (Fig. 2S).

To quantify if pO_2 during hypoxic pockets indeed reaches hypoxic threshold in cortex (≤ 18 mmHg)(15), we compared the pO_2(ΔB/B) decrease in hypoxic pockets with those during hypoxia (10% inhaled O_2) where pO_2 reached 11 mmHg (Fig. 1D). During hypoxia, pO_2(ΔB/B) was reduced by 29.2 ± 2.9%, similar to the decrease observed in hypoxic pockets (fig. S8A). Using the electrode and BLI correlation we determined that at a 20.6% ΔB/B reduction corresponds to the hypoxic threshold (fig. S8B).

Spectral absorption by hemoglobin is a common cause for artifacts in imaging fluorescent biosensors *in* vivo (16). To exclude the possible signal interference by hemoglobin as the underlying cause of the hypoxic pockets, we recorded the mNeonGreen fluorescence of GeNL instead (fig. S9A). Hemoglobin absorption should also affect the mNeonGreen fluorescence, which would be subject to hemoglobin absorption, but does not depend on O_2. However, no events with similar spatio-temporal characteristics as hypoxic pockets were observed in the mNeonGreen fluorescence traces (fig. S9B–E).

O_2 tension in and around venules is lower than in and around arterioles (17). We thus measured the distance of hypoxic pockets from arterioles and venules. Hypoxic pockets were closer to venules compared to arterioles with an average distance of 28.1 ± 0.7 μm and 48.0 ± 1.2 μm, respectively (fig. S10 A–C).

Tissue oxygenation is closely linked to the availability of O_2 and therefore to capillary circulation of red blood cells. We thus hypothesized that hypoxic pockets result from hemodynamic changes in the microcirculation. We used intrinsic optical spectroscopy imaging (IOSI) (12, 16) to monitor hemoglobin dynamics in the brain of resting awake mice (fig. S11A). Hemoglobin dynamics were recorded at the isosbestic point for total hemoglobin concentration ([HbT]) (fig. S11B). The analysis identified areas of low [HbT] which shared their characteristic onset and offset dynamics with hypoxic pockets measured with BLI (fig. S9C–F). On average 0.9 ± 0.01 events of low [HbT] were detected per mm^2 per second in IOSI measurements which lasted 16.5 ± 0.4 seconds covering 7344 ± 402 μm^2 (fig. S11G–J). During these events, [HbT] decreased by 1.9 ± 0.1 mmHg (fig. S11K). While bioluminescence allows only the measurement of tissue hypoxia, IOSI reflects blood volume and thus transient localized decreases of hemoglobin concentration with similar temporal and spatial properties as shown for hypoxic pockets.

Hypoxic pockets are manipulated by vasodilation and capillary stalling

Brain activity is accompanied by transient increases in blood flow due to vasodilation, a phenomenon called neurovascular coupling or functional hyperemia (18). We asked whether hyperemia suppresses the number of hypoxic pockets and induced vasodilation by increasing CO_2 in air (hypercapnia) (Fig. 3A) (9). The elevation of CO_2 in the inhaled air increased

Author Manuscript Author Manuscript Author Manuscript Author Manuscript

tissue pO_2 reversibly to 118.4 ± 0.3% concurrently with a sharp decrease in the number of hypoxic pockets per mm^2 per second in a reversible manner from 3.9 ± 0.1 to 2.3 ± 0.1 and back to 4.7 ± 0.1, a reduction of 41% when CO_2 was lowered (Fig. 3B–E). Area covered by hypoxic pockets changed by 0.54% from 1.01 ± 0.03% to 0.47 ± 0.02%, a reduction of 53% (Fig. 3F). pO_2(ΔB/B) decrease within hypoxic pockets during hypercapnia was reduced by 4% and stayed low after hypercapnia during the time of recording (Fig. 3G). Furthermore, the duration of hypoxic pockets was reduced by 17 seconds as well as their spatial expansion by 65% (Fig. 3H–I). After hypercapnia duration and size recovered (Fig. 3H–I). The observation is consistent with the finding that hypercapnia decreases the portion of poorly perfused capillaries in the rat brain cortex (19). To assess whether an increased acidification during hypercapnia is involved (20), we measured extracellular pH in the brain parenchyma during 10% CO_2 as described above. A five-minute period of 10% CO_2 decreased pHuji intensity by 6.4% in a reversible manner (fig. S12A–B). Typically, fluorescent proteins are quenched in acidic environments, yet we observed an increase in bioluminescence intensity during hypercapnia, excluding that the observation was an artificial effect of pH on the sensor's intensity.

Isoflurane is another potent vasodilator (21, 22) that increases blood volume but not tissue pH (23). We compared mice before and during isoflurane anesthesia and observed a decrease in the number of hypoxic pockets similar to CO_2 (fig. S13A–B). During isoflurane anesthesia the number of hypoxic pockets per second was effectively decreased from 6.2 ± 0.01 to 1.9 ± 0.03, a reduction of 69% (fig. S13C). The area covered by hypoxic pockets was reduced by 0.83%, a decrease of 13% (fig. S13 D). The pO_2(ΔB/B) decrease within hypoxic pockets was 21% less in isoflurane compared to awake mice and duration decreased by 15 seconds (fig. S13E–F). The size of hypoxic pockets was reduced by 13% (fig. S13 G).

A direct consequence of hypercapnia and isoflurane anesthesia-induced vasodilation is an increase in tissue pO_2 (13, 24). Increased tissue pO_2 might compensate for low-oxygenated areas increasing O_2 diffusion thus reducing prevalence of hypoxic pockets (25). To uncouple vasodilation and tissue oxygenation, we increased the O_2 in the inhalation air from 20% to 30% inducing hyperoxia (fig. S14A–C). This led to a 55% increase in ΔpO2 during hyperoxia which is substantially higher than measured under hypercapnia (fig. S14D). During hyperoxia the number of hypoxic pockets per second dropped from 3.5 ± 0.0.04 to 3.1 ± 0.03, a decrease of 11% (fig. S14E), which is far less compared to the isoflurane and hypercapnia conditions where hypoxic pockets were reduced by 69% and 41%, respectively. During hyperoxia pO_2(ΔB/B) in hypoxic pockets decreased 15.9% less compared to normoxia (fig. S14F), which might be explained by the accompanying increase in pO_2 leading to an overall increased tissue pO_2 reducing the amplitude of the hypoxic pockets. Furthermore, the duration of hypoxic pockets was reduced by 13 s (41.5 ± 1 vs 28.5 ± 1) and their size increased slightly by 13% (fig. S14G–H). These observations show that vasodilation more potently controls the hypoxic pockets than blood oxygenation.

Local cerebral microcirculation is mainly regulated by changes of vascular resistance (26). Reversible adhesion of circulating leukocytes can effectively cease capillary blood flow, a phenomenon termed as capillary stalling (27). To directly test whether capillary stalling elicits hypoxic pockets, microspheres (diameter: 4 μm) were delivered intravascularly (Fig.

Author Manuscript Author Manuscript Author Manuscript Author Manuscript

3J) to occlude capillaries (28, 29). We recorded O_2 dynamics and microspheres in the same field of view simultaneously at 1 Hz using a hybrid BLI-fluorescence microscope that utilizes the readout time of the BLI camera to record microsphere fluorescence with a second camera (Fig. 3K–M). Following injection of microspheres, the number of hypoxic pockets decreased from 8.2 ± 0.07 to 5.9 ± 0.06 (Fig. 3N). In contrast, the total area covered by hypoxic pockets per second increased from 2.4 to 5.9%, an increase of 146% (Fig. 3O). While $pO_2(\Delta B/B)$ only marginally changed (Fig. 3P), the duration of microsphere-induced hypoxic pockets was 11 seconds shorter (Fig. 3Q). Microsphere-induced hypoxic pockets were 445% larger than in the control group (Fig. 3R). Taken together, upon microsphere injection the area of hypoxic tissue was increased reflected an increase in size, but not in the number of pockets. A plausible explanation for this observation is that upon microsphere injection hypoxic pockets near each may fused together thus decreasing the number of individually detected events. When interrogating the dynamics of individual spheres and local tissue O_2 dynamics, it was clear that influx of a microsphere quickly triggered a local decrease in pO_2 with a similar temporal dynamic as the spontaneously occurring hypoxic pockets. (Fig. 3 S–X).

Hypoxic pockets are reduced by wakefulness and further suppressed by locomotion

To detect O_2 dynamics in awake animals and assess the effect of locomotion, mice were trained to tolerate head restraint. One group of awake mice was recorded on a stationary platform, whereas a second group of mice was placed on a polystyrene ball allowing head fixed locomotion (Fig. 4A). The number of hypoxic pockets in behaving mice was reduced by 17% compared to KX-anesthetized mice (Fig. 4B–D–F). Yet, the pockets increased in surface area by 41% (Fig. 4J). Hypoxic pockets lasted on average 8 s shorter in awake mice, whereas the amplitude was unaffected (Fig. 4 H–I). Taken together, the pO_2 maintains the same characteristics but is more dynamic in the awake than the anesthetized state possibly reflecting the higher level of neuronal activity and thereby blood flow in wakefulness compared with anesthesia (30, 31). We asked if the number of hypoxic pockets correlates with mice actively running, where increased blood flow and tissue pO_2 is expected (32). 24 hours after surgery, mice were placed on an air-supported polystyrene ball (33) and pO_2 dynamics were recorded (Fig. 4A–C). Compared to immobilized wake mice, number of hypoxic pockets was reduced by 35%, from 6.7 ± 0.05 to 4.3 ± 0.03, and percentage of area covered by hypoxia at any given time was reduced by 33% (Fig. 4D–G). On average, hypoxic pockets were 7 s shorter in mice who can freely run (Fig. 4H). Further, the amplitude of hypoxic pockets was dampened by 10.4% compared to immobilized mice (Fig. 4I). The spatial coverage of the hypoxic pockets was further reduced by 26% in running mice compared with immobile (Fig. 4J), while the number of ROIs of hypoxic pockets did not differ between KX-anesthetized, mobile, and immobile mice (Fig. 4K). The decrease of hypoxic pockets during active locomotion is unlikely due to a general increase in blood flow, as their highly structured spatial characterization is preserved, which is in contrast to the expected general linear increase in blood flow. We summarized the burden of hypoxic pockets on the brain as a measure of the effect of area, duration, and amplitude (Fig. 4L). Compared to quiet wakefulness, the analysis showed that the hypoxic burden

Author Manuscript Author Manuscript Author Manuscript Author Manuscript

is reduced by 52% in running mice (Fig. 4M). Earlier studies have shown that sensory stimulation can reduce prevalence of capillary stalls (25). To test whether a similar paradigm suppresses the occurrence of hypoxic pockets, a series of ten whisker stimulations were delivered to anesthetized mice (fig. S15 A). The stimulation resulted in a decrease in the number of hypoxic pockets by 35% (fig. S15B–H). Thus, functional hyperemia suppressed the occurrence of hypoxic pockets, whether initiated by sensory stimulation in anesthetized mice or by active running in awake behaving mice (fig. S15 I–M).

Discussion

This study shows that relative changes in pO_2 can be monitored continuously in wide cortical regions of awake behaving mice by a genetically encoded bioluminescent oxygen indicator. By monitoring the bioluminescence signal of GeNL expressed in astrocytes, we found that cortical pO_2 constantly fluctuates during physiological conditions giving rise to spatially and temporally defined hypoxic pockets. Manipulations that either increased or blocked capillary flow showed that local interruption of the microcirculation is responsible for the occurrence of hypoxic pockets. This conclusion was supported by imaging of cortical hemoglobin absorption, i.e., intrinsic optical signal (IOSI). Monitoring of the local hemoglobin concentration identified transient local reduction in hemoglobin, which shared their characteristic onset and offset dynamics with hypoxic pockets, thus providing an alternative approach to validate the occurrence of spatially restricted pO_2 fluctuations during physiological conditions.

Two-photon imaging of cortical capillaries has documented that the velocity of red blood cell can vary by more than a factor of 10 (34–36). A conserved evolutionary feature of the mammalian cortex is that the ratio of arterioles and venules is not one. A modelling study predicted that low-flow regions are inevitable due to the many sources and sinks of blood flow and tend to form around whichever vessel is more numerous (37). In contrast to humans where the ratio is 2.5:1 (arterioles:venules), in mice, venules outnumber arterioles by a factor of 2.6 (38), which is expected to increase the low-flow regions preferentially around venules. Indeed, our analysis supported this notion by demonstrating that hypoxic pockets tend to appear closer to venules compared to arterioles in mouse cortex.

We expressed GeNL under an astrocytic promoter to take advantage of that the fine astrocytic processes infiltrate all parts of the neuropil (39, 40). However, we do not expect that the astrocyte selective expression of GeNL had significant impact upon the observations. Oxygen diffuses freely across the neuropil with no restrictions imposed by either plasma membranes or by specific cell types (41, 42).

Why have hypoxic pockets not been detected earlier? Recording pO_2 concentration with a temporal resolution of 225 – 400 seconds per frame found hypoxic micro-pockets in the cortex of awake old mice using the phosphorescence probe, PtP-C343 (43, 44). However, the more frequent hypoxic events reported lasted only ~50 seconds and cannot be detected when imaging with a slow, minute lasting temporal resolution. Recently, 1/f-like fluctuations in pO_2 have been observed using Clark electrodes and linked to RBC spacing heterogeneity, in line with our observations (45). However, pO_2 declines in aging (43, 46) and it would be

Author Manuscript Author Manuscript Author Manuscript Author Manuscript

of interest to use the pO_2 bioluminescence imaging introduced here to assess whether aging is linked to progressive increase in the duration and/or spatial expansion of hypoxic pockets. Another open question is whether the transient hypoxic pockets contribute to the noise observed in the functional magnetic resonance imaging (fMRI) BOLD signal. The hypoxic pockets are below the spatial resolution of fMRI but are likely contributing to the significant noise during rest (47). It is in this regard of interest that our analysis showed that the burden of the hypoxic pockets decreased when neuronal activity was increased suggesting that the increase BOLD signal may in part reflect a drop in occurrence of hypoxic pockets. This conclusion is supported by the finding that increase in capillary blood flow reduces the relative portion of capillary stalls (19).

Monitoring pO_2 with BLI is limited to detection of short-term fluctuations, excelling at measuring relative changes over periods of minutes rather than providing accurate baseline pO_2 comparisons over extended durations or across groups. It is important to note that while BLI is effective for assessing relative pO_2, it does not offer absolute quantification.

Capillary blood flow is essential for supplying the brain with O_2 and glucose needed to support the high metabolic demand associated with normal brain function (48). Numerous studies have shown a link between reduced cerebral blood flow and cognitive decline (49–52), including changes in microvasculature structure and flow (29, 43). The existence of non-perfused capillaries were discovered decades ago (53) More recently, transient disruptions of flow, caused by neutrophil adhesion, at the single capillary level were identified as a potential mechanism that contributes to cerebral blood flow changes driving neurological deficits (54, 55). Increased capillary stalling has been observed in models of Alzheimer's disease (AD) (54), raising questions about the long-term impact of capillary stalling and its potential role in long-term neuronal viability. Hypoxia-induced increase in expression of hypoxia inducible factor 1a (HIF1a) impairs plasticity by disrupting synaptic physiology and spatial memory (56). Our study predicts that physical inactivity has direct effects on tissue pO_2 by favoring capillary occlusions and increasing the number of hypoxic pockets (fig. S16). Conversely, simply increasing sensory input or locomotion rapidly suppress the occurrence of hypoxic pockets perhaps explaining the linkage between sedentary lifestyle and an increased risk of dementia (57, 58).

Supplementary Material

Refer to Web version on PubMed Central for supplementary material.

Acknowledgments:

We thank Drs T. Nagai and S. Inagaki (Department of Biomolecular Science and Engineering, The Institute of Scientific and Industrial Research, Osaka University, Japan) for providing GeNL plasmid and helpful technical discussion. We further thank Dan Xue for assistance with the illustrations, Yue Zhao for assistance with the data repository, and Steve Goldman for comments on the manuscript.

Funding:

Dr Miriam and Sheldon G. Adelson Medical Research Foundation (MN)

National Institutes of Health grant R01AT012312 (MN)

Author Manuscript Author Manuscript Author Manuscript Author Manuscript

NINDS R01AT011439 (MN)

NCCIH U19 NS128613 (MN)

NHLBI R01HL122578 (MN)

Simons Foundation (MN)

Career Award at the Scientific Interface from Burroughs Wellcome Fund (MN)

JPND (MN)

Novo Nordisk Foundation NNF19OC0058058 (HH)

Lundbeck Foundation (VU)

Independent Research Fund Denmark 0134-00107B (HH)

Independent Research Fund Denmark 3101-00282B (MN)

US Army Research Office grants MURI W911NF1910280 (MN)

PARP W81XWH-16-1-0555 (MN)

PRAP W81XWH-22-1-0676 (MN)

Marie Skłodowska-Curie Fellowship ANCoDy, #101064009 (AA)

ONO Rising Star Fellowship (AA)

Data and materials availability:

The microscope recordings are available at the DANDI archive: https://doi.org/10.48324/dandi.000891/0.240215.0831. All other data are available in the manuscript or supplementary materials.

References and Notes

1. Kety SS, “THE GENERAL METABOLISM OF THE BRAIN *IN VIVO*” in Metabolism of the Nervous System, Richter D, Ed. (Pergamon, 1957), pp. 221–237.
2. Clarke DD, Sokoloff L, “Cerebral Energy Metabolism In Vivo” in Basic Neurochemistry: Molecular, Cellular and Medical Aspects. 6th Edition (Lippincott-Raven, 1999).
3. Rolfe DF, Brown GC, Cellular energy utilization and molecular origin of standard metabolic rate in mammals. Physiol Rev 77, 731–758 (1997). [PubMed: 9234964]
4. Takano T, Tian G-F, Peng W, Lou N, Lovatt D, Hansen AJ, Kasischke KA, Nedergaard M, Cortical spreading depression causes and coincides with tissue hypoxia. Nat Neurosci 10, 754–762 (2007). [PubMed: 17468748]
5. Li B, Esipova TV, Sencan I, Kılıç K, Fu B, Desjardins M, Moeini M, Kura S, Yaseen MA, Lesage F, Østergaard L, Devor A, Boas DA, Vinogradov SA, Sakadžić S, More homogeneous capillary flow and oxygenation in deeper cortical layers correlate with increased oxygen extraction. eLife 8, e42299 (2019). [PubMed: 31305237]
6. Hall MP, Unch J, Binkowski BF, Valley MP, Butler BL, Wood MG, Otto P, Zimmerman K, Vidugiris G, Machleidt T, Robers MB, Benink HA, Eggers CT, Slater MR, Meisenheimer PL, Klaubert DH, Fan F, Encell LP, Wood KV, Engineered luciferase reporter from a deep sea shrimp utilizing a novel imidazopyrazinone substrate. ACS Chem Biol 7, 1848–57 (2012). [PubMed: 22894855]
7. Suzuki K, Kimura T, Shinoda H, Bai G, Daniels MJ, Arai Y, Nakano M, Nagai T, Five colour variants of bright luminescent protein for real-time multicolour bioimaging. Nat Commun 7, 13718 (2016). [PubMed: 27966527]

Author Manuscript Author Manuscript Author Manuscript Author Manuscript

8. Lambrechts D, Roeffaers M, Goossens K, Hofkens J, de Putte TV, Schrooten J, Oosterwyck HV, A Causal Relation between Bioluminescence and Oxygen to Quantify the Cell Niche. PLOS ONE 9, e97572 (2014). [PubMed: 24840204]

9. Pollock RA, Jackson RT, Clairmont AA, Nicholson WL, Carbon Dioxide as an Otic Vasodilator: Otic Blood Flow as Measured by the Microsphere Technique. Archives of Otolaryngology 100, 309–313 (1974). [PubMed: 4412310]

10. Lee J, Taira T, Pihlaja P, Ransom BR, Kaila K, Effects of CO2 on excitatory transmission apparently caused by changes in intracellular pH in the rat hippocampal slice. Brain Res 706, 210–216 (1996). [PubMed: 8822358]

11. Shen Y, Rosendale M, Campbell RE, Perrais D, pHuji, a pH-sensitive red fluorescent protein for imaging of exo- and endocytosis. Journal of Cell Biology 207, 419–432 (2014). [PubMed: 25385186]

12. Holstein-Rønsbo S, Gan Y, Giannetto MJ, Rasmussen MK, Sigurdsson B, Beinlich FRM, Rose L, Untiet V, Hablitz LM, Kelley DH, Nedergaard M, Glymphatic influx and clearance are accelerated by neurovascular coupling. Nat Neurosci 26, 1042–1053 (2023). [PubMed: 37264158]

13. Lyons DG, Parpaleix A, Roche M, Charpak S, Mapping oxygen concentration in the awake mouse brain. eLife 5, e12024 (2016). [PubMed: 26836304]

14. Aydin A-K, Verdier C, Chaigneau E, Charpak S, The oxygen initial dip in the brain of anesthetized and awake mice. Proceedings of the National Academy of Sciences 119, e2200205119 (2022).

15. Xu K, Boas DA, Sakadžić S, LaManna JC, Brain Tissue PO2 Measurement During Normoxia and Hypoxia Using Two-Photon Phosphorescence Lifetime Microscopy. Advances in experimental medicine and biology 977, 149 (2017). [PubMed: 28685439]

16. Ma Y, Shaik MA, Kozberg MG, Kim SH, Portes JP, Timerman D, Hillman EMC, Resting-state hemodynamics are spatiotemporally coupled to synchronized and symmetric neural activity in excitatory neurons. Proceedings of the National Academy of Sciences 113, E8463–E8471 (2016).

17. Zhu X, Huang Q, DiSpirito A, Vu T, Rong Q, Peng X, Sheng H, Shen X, Zhou Q, Jiang L, Hoffmann U, Yao J, Real-time whole-brain imaging of hemodynamics and oxygenation at micro-vessel resolution with ultrafast wide-field photoacoustic microscopy. Light Sci Appl 11, 138 (2022). [PubMed: 35577780]

18. Nippert AR, Biesecker KR, Newman EA, Mechanisms Mediating Functional Hyperemia in the Brain. Neuroscientist 24, 73–83 (2018). [PubMed: 28403673]

19. Villringer A, Them A, Lindauer U, Einhäupl K, Dirnagl U, Capillary perfusion of the rat brain cortex. An in vivo confocal microscopy study. Circ Res 75, 55–62 (1994). [PubMed: 8013082]

20. Brodie DA, Woodbury DM, Acid-Base Changes in Brain and Blood of Rats Exposed to High Concentrations of Carbon Dioxide. American Journal of Physiology-Legacy Content 192, 91–94 (1957).

21. Cucchiara RF, Theye RA, Michenfelder JD, The Effects of Isoflurane on Canine Cerebral Metabolism and Blood Flow. Anesthesiology 40, 571–574 (1974). [PubMed: 4829725]

22. Gelman S, Fowler KC, Smith LR, Regional Blood Flow during Isoflurane and Halothane Anesthesia. Anesthesia & Analgesia 63, 557 (1984). [PubMed: 6731876]

23. Low LA, Bauer LC, Klaunberg BA, Comparing the Effects of Isoflurane and Alpha Chloralose upon Mouse Physiology. PLoS One 11, e0154936 (2016). [PubMed: 27148970]

24. Aksenov D, Eassa JE, Lakhoo J, Wyrwicz A, Linsenmeier RA, Effect of isoflurane on brain tissue oxygen tension and cerebral autoregulation in rabbits. Neuroscience Letters 524, 116–118 (2012). [PubMed: 22824303]

25. Erdener ŞE, Tang J, Sajjadi A, Kılıç K, Kura S, Schaffer CB, Boas DA, Spatio-temporal dynamics of cerebral capillary segments with stalling red blood cells. J Cereb Blood Flow Metab 39, 886–900 (2019). [PubMed: 29168661]

26. Iadecola C, The Neurovascular Unit Coming of Age: A Journey through Neurovascular Coupling in Health and Disease. Neuron 96, 17–42 (2017). [PubMed: 28957666]

27. Bracko O, Cruz Hernández JC, Park L, Nishimura N, Schaffer CB, Causes and consequences of baseline cerebral blood flow reductions in Alzheimer's disease. J Cereb Blood Flow Metab 41, 1501–1516 (2021). [PubMed: 33444096]

Author Manuscript Author Manuscript Author Manuscript Author Manuscript

28. Reeson P, Schager B, Van Sprengel M, Brown CE, Behavioral and Neural Activity-Dependent Recanalization of Plugged Capillaries in the Brain of Adult and Aged Mice. Frontiers in Cellular Neuroscience 16 (2022).
29. Reeson P, Choi K, Brown CE, VEGF signaling regulates the fate of obstructed capillaries in mouse cortex. eLife 7, e33670 (2018). [PubMed: 29697373]
30. Greenberg DS, Houweling AR, Kerr JND, Population imaging of ongoing neuronal activity in the visual cortex of awake rats. Nat Neurosci 11, 749–751 (2008). [PubMed: 18552841]
31. Masamoto K, Obata T, Kanno I, Intracortical microcirculatory change induced by anesthesia in rat somatosensory cortex. Adv Exp Med Biol 662, 57–61 (2010). [PubMed: 20204771]
32. Zhang Q, Roche M, Gheres KW, Chaigneau E, Kedarasetti RT, Haselden WD, Charpak S, Drew PJ, Cerebral oxygenation during locomotion is modulated by respiration. Nat Commun 10, 5515 (2019). [PubMed: 31797933]
33. Untiet V, Beinlich FRM, Kusk P, Kang N, Ladron-de-Guevara A, Song W, Kjaerby C, Andersen M, Hauglund N, Bojarowska Z, Sigurdsson B, Deng S, Hirase H, Petersen NC, Verkhratsky A, Nedergaard M, Astrocytic chloride is brain state dependent and modulates inhibitory neurotransmission in mice. Nat Commun 14, 1871 (2023). [PubMed: 37015909]
34. Chaigneau E, Oheim M, Audinat E, Charpak S, Two-photon imaging of capillary blood flow in olfactory bulb glomeruli. Proc Natl Acad Sci U S A 100, 13081–6 (2003). [PubMed: 14569029]
35. Wei HS, Kang H, Rasheed I-YD, Zhou S, Lou N, Gershteyn A, McConnell ED, Wang Y, Richardson KE, Palmer AF, Xu C, Wan J, Nedergaard M, Erythrocytes Are Oxygen-Sensing Regulators of the Cerebral Microcirculation. Neuron 91, 851–862 (2016). [PubMed: 27499087]
36. Grutzendler J, Nedergaard M, Cellular Control of Brain Capillary Blood Flow: In Vivo Imaging Veritas. Trends Neurosci 42, 528–536 (2019). [PubMed: 31255380]
37. Qi Y, Roper M, Control of low flow regions in the cortical vasculature determines optimal arterio-venous ratios. Proceedings of the National Academy of Sciences 118, e2021840118 (2021).
38. Blinder P, Tsai PS, Kaufhold JP, Knutsen PM, Suhl H, Kleinfeld D, The cortical angiome: an interconnected vascular network with noncolumnar patterns of blood flow. Nat Neurosci 16, 889–97 (2013). [PubMed: 23749145]
39. Ogata K, Kosaka T, Structural and quantitative analysis of astrocytes in the mouse hippocampus. Neuroscience 113, 221–233 (2002). [PubMed: 12123700]
40. Bushong EA, Martone ME, Jones YZ, Ellisman MH, Protoplasmic Astrocytes in CA1 Stratum Radiatum Occupy Separate Anatomical Domains. J. Neurosci 22, 183–192 (2002). [PubMed: 11756501]
41. Kasischke KA, Lambert EM, Panepento B, Sun A, Gelbard HA, Burgess RW, Foster TH, Nedergaard M, Two-Photon NADH Imaging Exposes Boundaries of Oxygen Diffusion in Cortical Vascular Supply Regions. J Cereb Blood Flow Metab 31, 68–81 (2011). [PubMed: 20859293]
42. Krogh A, The number and distribution of capillaries in muscles with calculations of the oxygen pressure head necessary for supplying the tissue. The Journal of Physiology 52, 409–415 (1919). [PubMed: 16993405]
43. Moeini M, Lu X, Avti PK, Damseh R, Bélanger S, Picard F, Boas D, Kakkar A, Lesage F, Compromised microvascular oxygen delivery increases brain tissue vulnerability with age. Sci Rep 8, 8219 (2018). [PubMed: 29844478]
44. Lu X, Moeini M, Li B, de Montgolfier O, Lu Y, Bélanger S, Thorin É, Lesage F, Voluntary exercise increases brain tissue oxygenation and spatially homogenizes oxygen delivery in a mouse model of Alzheimer's disease. Neurobiology of Aging 88, 11–23 (2020). [PubMed: 31866158]
45. Zhang Q, Gheres KW, Drew PJ, Origins of 1/f-like tissue oxygenation fluctuations in the murine cortex. PLOS Biology 19, e3001298 (2021). [PubMed: 34264930]
46. Mathiesen C, Brazhe A, Thomsen K, Lauritzen M, Spontaneous Calcium Waves in Bergman Glia Increase with Age and Hypoxia and may Reduce Tissue Oxygen. J Cereb Blood Flow Metab 33, 161–169 (2013). [PubMed: 23211964]
47. Kim S-G, Ogawa S, Biophysical and Physiological Origins of Blood Oxygenation Level-Dependent fMRI Signals. J Cereb Blood Flow Metab 32, 1188–1206 (2012). [PubMed: 22395207]
48. Iadecola C, The Pathobiology of Vascular Dementia. Neuron 80, 844–866 (2013). [PubMed: 24267647]

Author Manuscript Author Manuscript Author Manuscript Author Manuscript

49. Iturria-Medina Y, Sotero RC, Toussaint PJ, Mateos-Pérez JM, Evans AC, Early role of vascular dysregulation on late-onset Alzheimer's disease based on multifactorial data-driven analysis. Nat Commun 7, 11934 (2016). [PubMed: 27327500]
50. de la Torre JC, Alzheimer disease as a vascular disorder: nosological evidence. Stroke 33, 1152–1162 (2002). [PubMed: 11935076]
51. Kalaria RN, The role of cerebral ischemia in Alzheimer's disease. Neurobiol Aging 21, 321–330 (2000). [PubMed: 10867217]
52. Farkas E, Luiten PG, Cerebral microvascular pathology in aging and Alzheimer's disease. Prog Neurobiol 64, 575–611 (2001). [PubMed: 11311463]
53. Kuschinsky W, Paulson OB, Capillary circulation in the brain. Cerebrovasc Brain Metab Rev 4, 261–286 (1992). [PubMed: 1389958]
54. Cruz Hernández JC, Bracko O, Kersbergen CJ, Muse V, Haft-Javaherian M, Berg M, Park L, Vinarcsik LK, Ivasyk I, Rivera DA, Kang Y, Cortes-Canteli M, Peyrounette M, Doyeux V, Smith A, Zhou J, Otte G, Beverly JD, Davenport E, Davit Y, Lin CP, Strickland S, Iadecola C, Lorthois S, Nishimura N, Schaffer CB, Neutrophil adhesion in brain capillaries reduces cortical blood flow and impairs memory function in Alzheimer's disease mouse models. Nat Neurosci 22, 413–420 (2019). [PubMed: 30742116]
55. Erdener ŞE, Tang J, Kılıç K, Postnov D, Giblin JT, Kura S, Chen I-CA, Vayisoğlu T, Sakadžić S, Schaffer CB, Boas DA, Dynamic capillary stalls in reperfused ischemic penumbra contribute to injury: A hyperacute role for neutrophils in persistent traffic jams. J Cereb Blood Flow Metab 41, 236–252 (2021). [PubMed: 32237951]
56. Arias-Cavieres A, Khuu MA, Nwakudu CU, Barnard JE, Dalgin G, Garcia AJ, A HIF1a-Dependent Pro-Oxidant State Disrupts Synaptic Plasticity and Impairs Spatial Memory in Response to Intermittent Hypoxia. eNeuro 7, ENEURO.0024–20.2020 (2020).
57. Yan S, Fu W, Wang C, Mao J, Liu B, Zou L, Lv C, Association between sedentary behavior and the risk of dementia: a systematic review and meta-analysis. Transl Psychiatry 10, 112 (2020). [PubMed: 32317627]
58. Raichlen DA, Aslan DH, Sayre MK, Bharadwaj PK, Ally M, Maltagliati S, Lai MHC, Wilcox RR, Klimentidis YC, Alexander GE, Sedentary Behavior and Incident Dementia Among Older Adults. JAMA 330, 934–940 (2023). [PubMed: 37698563]
59. Schindelin J, Arganda-Carreras I, Frise E, Kaynig V, Longair M, Pietzsch T, Preibisch S, Rueden C, Saalfeld S, Schmid B, Tinevez J-Y, White DJ, Hartenstein V, Eliceiri K, Tomancak P, Cardona A, Fiji: an open-source platform for biological-image analysis. Nat Methods 9, 676–682 (2012). [PubMed: 22743772]
60. Gundersen JK, Ramsing NB, Glud RN, Predicting the signal of O2 microsensors from physical dimensions, temperature, salinity, and O2 concentration. Limnology and Oceanography 43, 1932–1937 (1998).
61. Nasu Y, Aggarwal A, Le GNT, Vo CT, Kambe Y, Wang X, Beinlich FRM, Lee AB, Ram TR, Wang F, Gorzo KA, Kamijo Y, Boisvert M, Nishinami S, Kawamura G, Ozawa T, Toda H, Gordon GR, Ge S, Hirase H, Nedergaard M, Paquet M-E, Drobizhev M, Podgorski K, Campbell RE, Lactate biosensors for spectrally and spatially multiplexed fluorescence imaging. Nat Commun 14, 6598 (2023). [PubMed: 37891202]
62. Edelstein A, Amodaj N, Hoover K, Vale R, Stuurman N, Computer Control of Microscopes Using μManager. Current Protocols in Molecular Biology 92, 14.20.1–14.20.17 (2010).
63. Kjaerby C, Andersen M, Hauglund N, Untiet V, Dall C, Sigurdsson B, Ding F, Feng J, Li Y, Weikop P, Hirase H, Nedergaard M, Memory-enhancing properties of sleep depend on the oscillatory amplitude of norepinephrine. Nat Neurosci 25, 1059–1070 (2022). [PubMed: 35798980]
64. Cantu DA, Wang B, Gongwer MW, He CX, Goel A, Suresh A, Kourdougli N, Arroyo ED, Zeiger W, Portera-Cailliau C, EZcalcium: Open-Source Toolbox for Analysis of Calcium Imaging Data. Frontiers in Neural Circuits 14 (2020).
65. Turner KL, Gheres KW, Proctor EA, Drew PJ, Neurovascular coupling and bilateral connectivity during NREM and REM sleep. eLife 9, e62071 (2020). [PubMed: 33118932]

Author Manuscript Author Manuscript Author Manuscript Author Manuscript

66. Yu Z, Guindani M, Grieco SF, Chen L, Holmes TC, Xu X, Beyond t test and ANOVA: applications of mixed-effects models for more rigorous statistical analysis in neuroscience research. Neuron 110, 21–35 (2022). [PubMed: 34784504]

Author Manuscript Author Manuscript Author Manuscript Author Manuscript

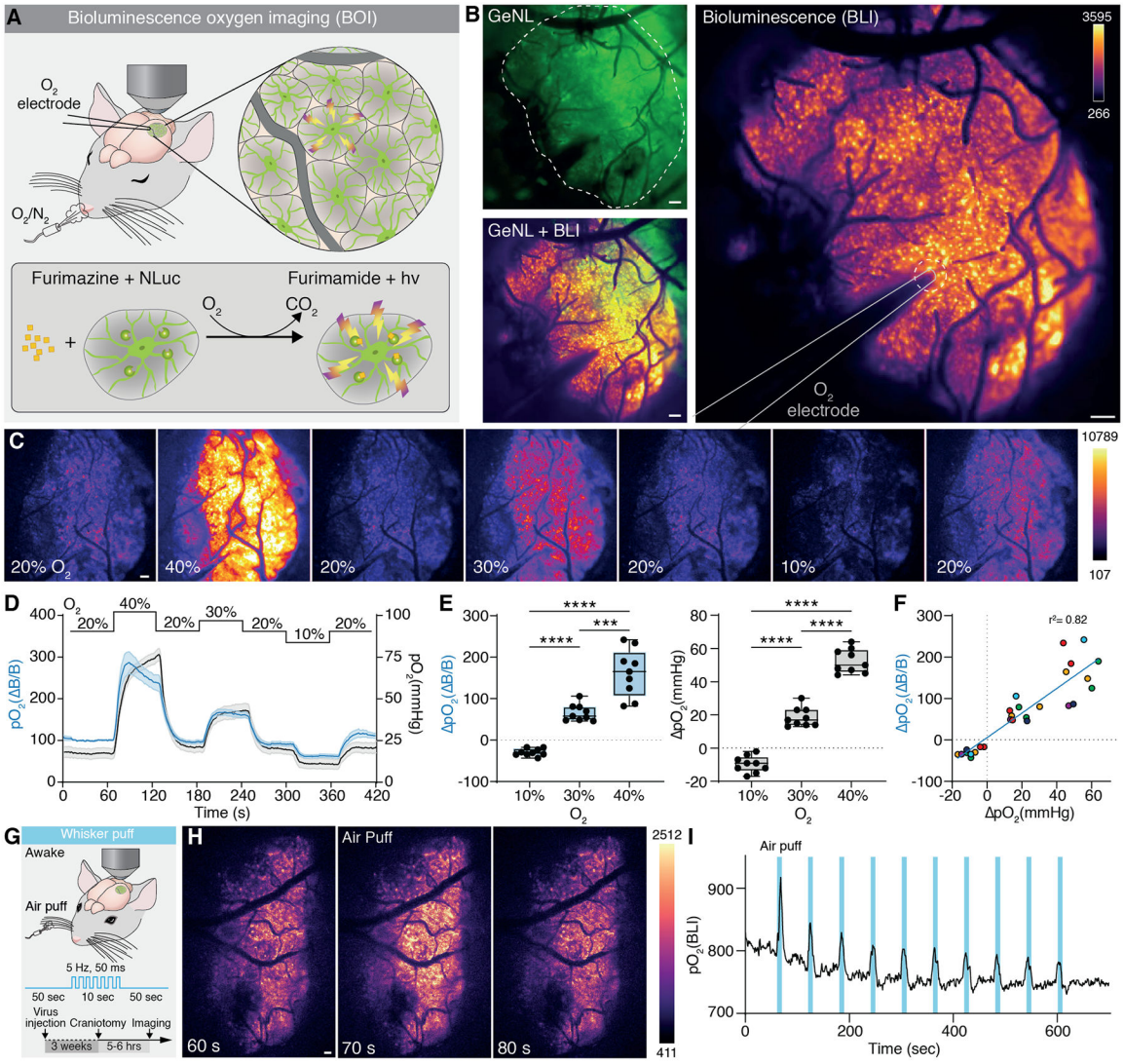

Fig. 1. Bioluminescence intensity of GeNL reports cerebral partial oxygen pressure.

(A) Top: Scheme of the experimental setup. Ketamine/Xylazine (KX) anesthetized mice expressing GeNL under GFAP promoter were placed under a macroscope and exposed to different O_2 concentrations. An O_2-sensitive microelectrode was inserted into the cortex through an acute craniotomy and aCSF supplemented with furimazine (0.25 mM). Bottom: Chemical reaction of furimazine to furimamide catalyzed by GeNL under presence of O_2 leading to light output in form of bioluminescence. **(B)** Overlay of BLI and mNeonGreen fluorescence exited at 490 nm. Dashed line outlines the craniotomy; straight line outlines the oxygen-sensitive microelectrode. **(C)** BLI changes with varying concentrations of O_2 in the inhaled air. Single frames (1 second exposure time) at indicated O_2 concentrations throughout the calibration protocol. **(D)** Mean trace of the BLI and pO_2 as measured with the O_2 electrode at varying O_2 concentration. Shade area indicates standard error. **(E)** BLI intensity ($pO_2(\Delta B/B)$) changes 162 % (± 19.13 SEM) when O_2 concentration in the tidal air is doubled. A 10 % increase in O_2 induces a 66 % (± 6.70) increase. Under hypoxia BLI is reduced by 29 % (± 2.91). Accordingly, pO_2 increases by 52.4 mmHg (± 2.4) when O_2

Author Manuscript Author Manuscript Author Manuscript Author Manuscript

concentration is doubled. A 10 % increase in O_2 increases pO_2 by 18.6 mmHg (±1.9), a 10 % decrease reduces pO_2 by 9.7 mmHg (±1.6). Left panel: One-way Repeated measures ANOVA $F_{1.272, 10.18} = 82.66$, $p<0.0001$ main effect of group. Tukey post hoc: 10% vs 30%, $p<0.0001$; 10% vs 40%, $p<0.000$; 30% vs 40%, $p=0.0006$. Right panel: One-way Repeated measures ANOVA $F_{1.523, 12.18} = 219.7$, $p<0.0001$ main effect of group. Tukey post hoc: 10% vs 30%, $p<0.0001$; 10% vs 40%, $p<0.000$; 30% vs 40%, $p<0.0001$. **(F)** Dependency of change in BLI and corresponding change in pO_2 recorded with the O_2 electrode in the same region upon changes in O_2 concentration of the inhalation air. Data points are fitted with a linear regression with an r^2 of 0.82. Dots sharing the same color indicate data points from the same mouse. **(G)** Cerebral pO_2 was measured using BLI in somatosensory cortex of awake stationary head-fixed mice subjected to air-puff whisker stimulation **(H)** Images from single frames at indicated time points before, during, and after a whisker puff. **(I)** Trace of ΔpO_2 upon whisker stimulation showing elevated pO_2 during each of the 10 repetitions. Means ± SEM are shown; SEM = standard error of the mean. ***: $P < 0.001$, ****: $P < 0.0001$. **D-F**: $N = 9$ trials from 6 mice. Scale bars, 100 μm.

Author Manuscript Author Manuscript Author Manuscript Author Manuscript

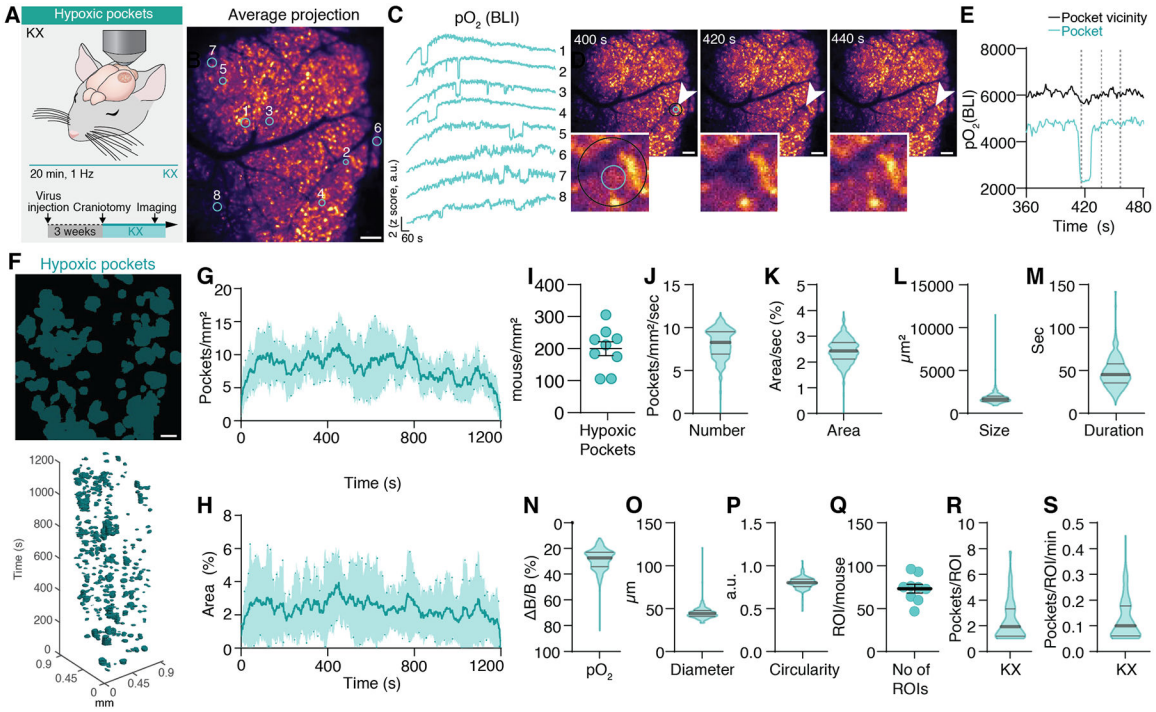

Fig. 2. Characterization of hypoxic pockets in cortex of anesthetized mice.

(A) Cerebral pO_2 was imaged in somatosensory cortex of KX anesthetized mice over 20 minutes using BLI. **(B)** Average projection of BLI of the mouse cortex expressing GeNL in astrocytes after furimazine administration from a 20-minute recording. **(C)** Time traces of the z-scored bioluminescent intensity of tissue pO_2. Numbers indicate corresponding region of interest from manually drawn circles in **B**. **(D)** Images recorded at 400, 420, and 440 seconds from **B**. Insert shows magnification of the region of interest indicated by arrows (2 from **C**). Inner circle defines area of pocket. The outer circle defines pocket vicinity. **(E)** Time trace of cerebral pO_2 from the region of interest indicated by cyan (inner) and black (outer) circle in **D**. **(F)** Top: Average distribution of hypoxic pockets from **B**. Bottom: Hypoxic pockets during KX anesthesia in the form of regions of interest over time displayed in a x-y-t 3D rendering. Cyan regions denote signal. **(G)** Line plot showing average number of hypoxic pockets per mm^2 per second over time. Shading indicates SEM. **(H)** Line plot showing average area of the field of view covered by hypoxic pockets for each frame. Shading indicates SEM. **(I)** Average number of detected hypoxic pockets per mm^2 per mouse in a recording session. **(J)** Frequency distribution of number of hypoxic pockets per second per mm^2. **(K)** Frequency distribution of area covered by hypoxic pockets per second. **(L)** Frequency distribution of size of hypoxic pockets. **(M)** Frequency distribution of duration of hypoxic pockets. **(N)** Frequency distribution of amplitude changes relative to baseline pO_2 of hypoxic pockets. **(O)** Frequency distribution of diameter of hypoxic pockets. **(P)** Frequency distribution of circularity of hypoxic pockets. **(Q)** Average number of active regions with reoccurring hypoxic pockets (ROIs) per mouse in a single recording session. **(R)** Frequency distribution of the number of hypoxic pockets for each detected active region. **(S)** Frequency distribution of the number of hypoxic pockets for each detected active region

per minute. $N = 9$ mice (8 recorded for 20 minutes, 1 for 10 minutes). SEM = standard error of the mean. Violin plots show median and quartiles. Scale bars, 100 μm.

Author Manuscript Author Manuscript Author Manuscript Author Manuscript

Author Manuscript Author Manuscript Author Manuscript Author Manuscript

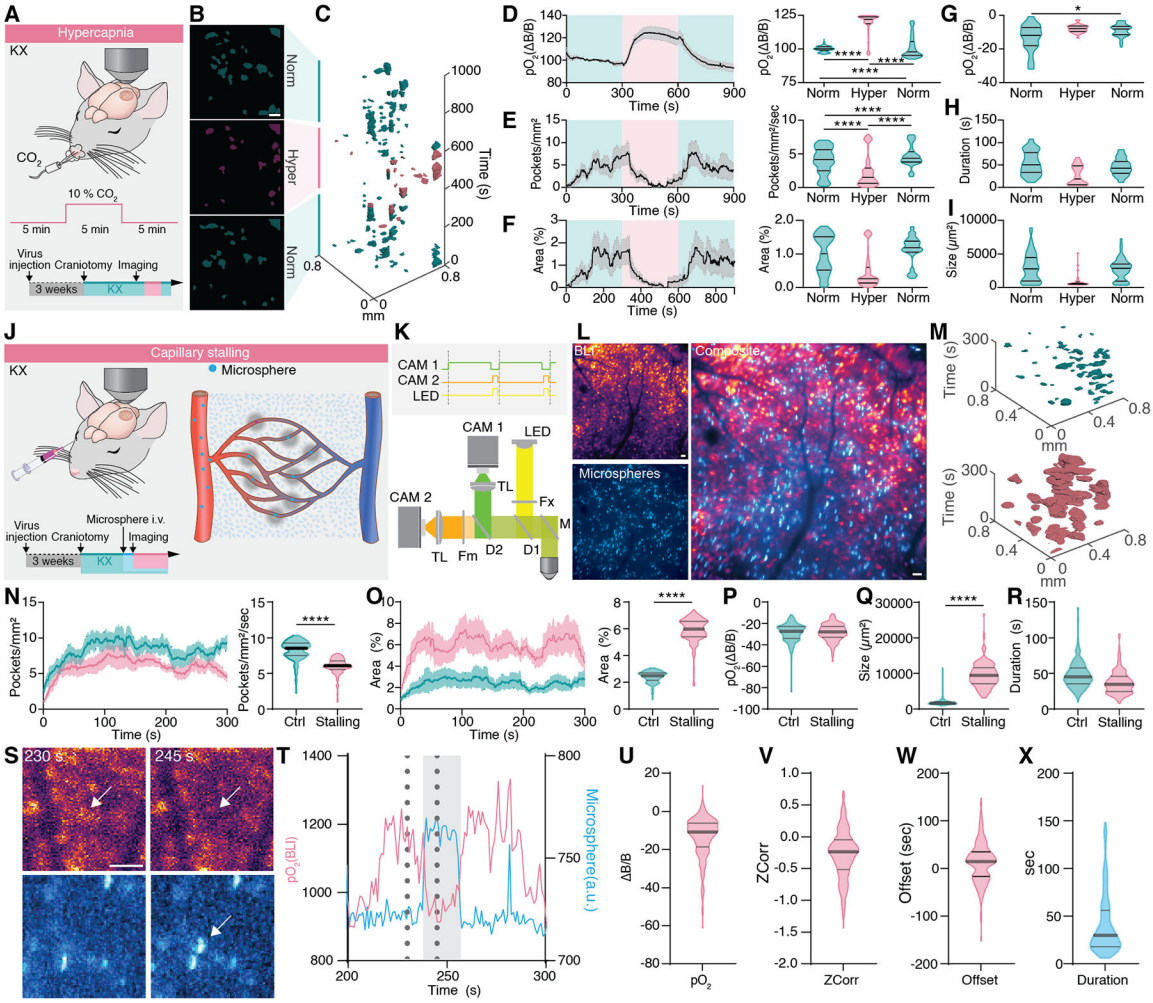

Fig. 3. Hypoxic pockets are manipulated by vasodilation and capillary stalling.

(A) Cerebral pO_2 was measured in KX anesthetized mice exposed to 10% CO_2 in the inhaled air for 10 minutes after acute craniotomy. **(B)** Averages of the location of hypoxic pockets, before, during and after hypercapnia. Norm = normocapnia, hyper = hypercapnia. **(C)** Hypoxic Pockets during transition to and from hypercapnia, respectively, in the form of regions of interest over time displayed in a x-y-t 3D rendering. Turquoise regions denote signal at normoxia, Lilac regions denote signal during hypercapnia. **(D)** Left: Average trace of cerebral pO_2 during the experiment. Lilac shade indicates the period of increased CO_2, Turquoise shade indicates periods of normal CO_2 levels. Right: Frequency distribution of pO_2 per second in a 5 min window before, during and after increased CO_2. **(E)** Left: Average trace of the number of hypoxic pockets per mm^2. Lilac shade indicates period of increased CO_2, turquoise shade indicates periods of normal CO_2 levels. Right: Frequency distribution of number of pockets per mm^2 per second before, during and after increased CO_2. **(F)** Left: Average trace of the area covered by hypoxic pockets. Lilac shade indicates period of increase CO_2, turquoise shade indicates periods of normal CO_2 levels. Right: Frequency distribution of area covered by hypoxic pockets per second in a 5 min window before, during and after increased CO_2. **(G)** Amplitude of hypoxic pockets before, during, and after CO_2

Author Manuscript Author Manuscript Author Manuscript Author Manuscript

increase. **(H)** Duration of hypoxic pockets before, during, and after CO_2 increase. **(I)** Size of hypoxic pockets before, during, and after CO_2 increase. **(J)** Cerebral pO_2 was measured with BLI in KX anesthetized mice. Capillary stalling was induced by intra-vascular injection of 4 μm microspheres before onset of imaging session. **(K)** The hybrid BLI-Fluorescence microscope setup used to image BLI and microsphere fluorescence simultaneously. **(L)** Left: Average intensity projection of BLI (top) and microsphere fluorescence (bottom). Right: Overlay of BLI and microsphere fluorescence. **(M)** Hypoxic pockets in the form of regions of interest over time displayed in a x-y-t 3D rendering. Turquoise regions denote signal under control and lilac regions denote signal after injection of microspheres. **(N)** Left: Average number of hypoxic pockets from control mice and after injection of microspheres. Shading indicates ± SEM. Right: Frequency distribution of number of hypoxic pockets per second in the cortex of control and microsphere injected mice. **(O)** Left: Average area covered by hypoxic pockets in control mice and mice injected with microspheres. Shading indicates ± SEM. Right: Frequency distribution of area covered by hypoxic pockets per second in the cortex of control and microsphere injected mice. (**P)** Amplitude of hypoxic pockets. **(Q)** Size of hypoxic pockets. **(R)** Duration of hypoxic pockets. **(S)** Images recorded at 230 and 245 seconds from **L**. Arrow indicate ROI. **(T)** Time trace of BLI (cyan) and microsphere fluorescence (green) from the ROI indicated by arrow in the **S**. Dotted lines indicate time points of images in **S**. Grey zone indicates time window where microsphere was visible. **(U)** Amplitude of BLI decrease during events where microspheres were stalled. **(V)** Correlation of BLI and microsphere fluorescence. **(W)** Offset between BLI decrease normalized to microsphere onset. **(X)** Duration of microsphere stalling. N = 6 mice hypercapnia. $N = 9$ mice control. $N = 5$ mice microsphere injection. Means ± SEM are shown. SEM = Standard error of the mean. Violin plots show median and quartiles. Bars indicating Tukey's *post-hoc* tests between groups at their edges: *: $P < 0.05$, **: $P < 0.01$, ***: $P < 0.001$, ****: $P < 0.0001$. Scale bars, 100 μm.

Author Manuscript Author Manuscript Author Manuscript Author Manuscript

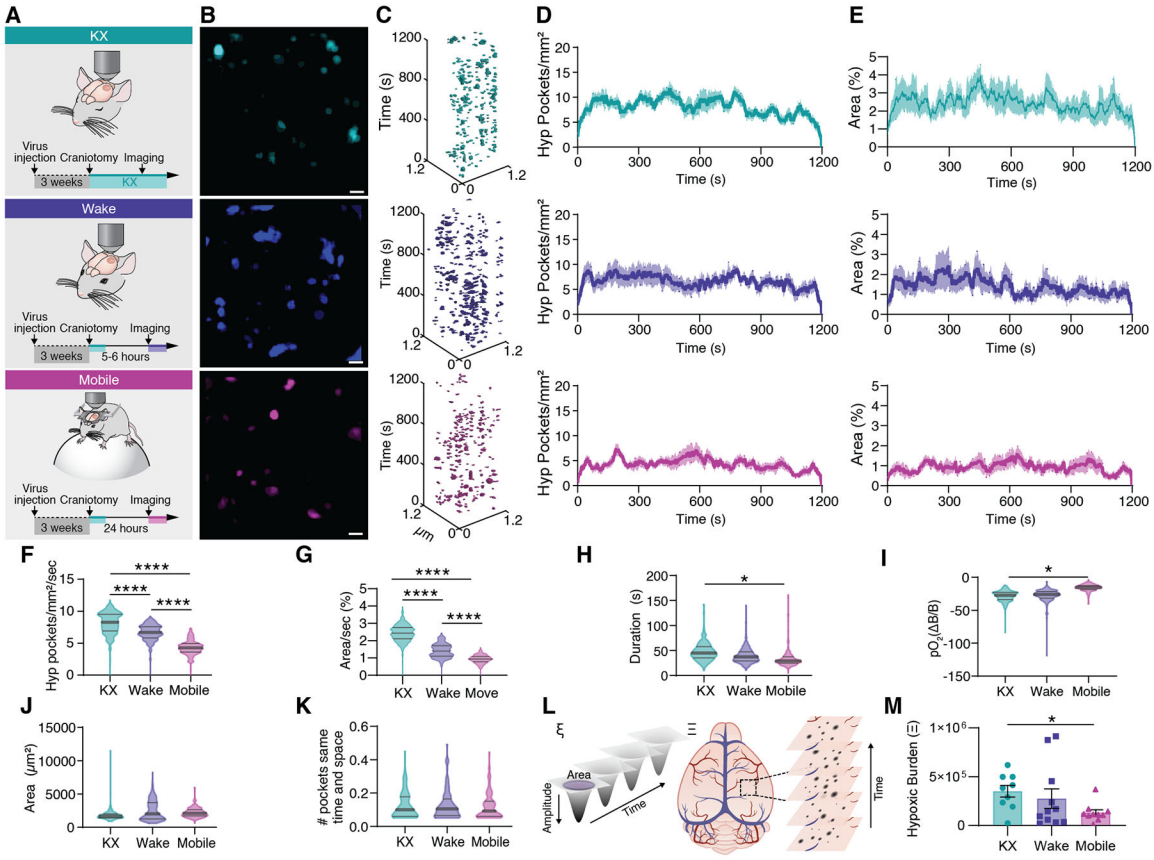

Fig. 4. Increased arousal level suppresses tissue hypoxia.

(A) Cerebral pO_2 was either measured in KX anesthetized mice, awake head-fixed mice during quiet wakefulness in a MAG-1 mouse holder or in mobile mice voluntarily running on a Styrofoam sphere. **(B)** Distribution of hypoxic pockets in a single recording session covering 20 minutes. **(C)** Hypoxic Pockets identified in **B** in the form of regions of interest over time displayed in an x-y-t 3D rendering. Turquoise regions denote signal. **(D)** Average number of hypoxic pockets detected for each frame in mice during KX anesthetized, wakefulness and mobile wakefulness, respectively. **(E)** Average area hypoxic pockets cover in the field of view in % detected for each frame in mice during KX anesthesia, wakefulness, and mobile wakefulness, respectively. **(F)** Frequency distribution of number of hypoxic pockets. **(G)** Frequency distribution of area covered by hypoxic pockets in the field of view per second. **(H)** Frequency distribution of duration of hypoxic pockets. **(I)** Frequency distribution of amplitude of hypoxic pockets. **(J)** Frequency distribution of size of hypoxic pockets. **(K)** Frequency distribution of number of hypoxic pockets sharing the same region per second. **(L)** Schematic illustrating the parameters used to calculate the hypoxic burden for each hypoxic pocket (left; ξ), and for an entire recording/mouse (right; Ξ). **(M)** Hypoxic burden during KX anesthesia, wakefulness, and mobile wakefulness. $N = 9$ mice KX, 11 mice wake, 10 mice mobile; Means ± SEM are shown. SEM = standard error of the mean. Violin plots show median and quartiles. Bars indicating Tukey's *post-hoc* tests between

groups at their edges: *: P < 0.05, P < 0.01, ***: P < 0.001, ****: P < 0.0001. Scale bars, 100 μm.

Author Manuscript Author Manuscript Author Manuscript Author Manuscript